



Silicon-based ultra-broadband mid-IR and LWIR near-perfect metamaterial absorber

Ahmed Elsayed Abouelez¹ · Essam A. Eldiwany¹ · Mohamed A. Swillam²

Received: 29 February 2024 / Accepted: 20 April 2024 / Published online: 21 May 2024
© The Author(s) 2024

Abstract

Ultra-broadband metamaterial absorbers (UBMAs) that are compatible with CMOS technology for use in the mid-infrared and long-wave infrared regions are crucial for a variety of applications, including radiative cooling, thermal photovoltaic, and thermal imaging. In this regard, we propose, in this work, a design of an UBMA based on the heavily doped silicon (D-Si) and silicon carbide (SiC). The 3D finite-difference time-domain method is used, mainly, to numerically calculate the optical characteristics of the proposed UBMA. The absorber, which is made up of a periodic array of symmetrical multilayered square rings of D-Si and SiC, achieves high absorption with an average absorption of 95% over a wavelength range of 2.5–22 μm . This broad range of wavelength absorption is attained, encompassing the mid-, long-wave, and partial far-infrared regions. In addition to the materials' inherent absorption, the stimulation of magnetic polaritons, surface plasmon polaritons, localized surface plasmon resonance, and cavity resonance are responsible for the nearly perfect broadband absorption. Under normal incidence, the proposed UBMA is polarization-independent due to the symmetrical design of the absorber. Furthermore, the impact of the incidence angle on the absorption of transverse electric and transverse magnetic waves is examined.

Keywords Doped silicon · Silicon carbide · Mid-infrared · Long-wave infrared · Metamaterials · Absorbers

1 Introduction

Engineered materials known as metamaterials are composed of periodic subwavelength metallic/dielectric structures that possess unusual electromagnetic properties not present in natural materials. These materials offer a highly flexible operating range, excellent absorption efficiency, and ultra-thin dimensions. They, therefore, have a wide range of applications including electromagnetic wave absorption, imaging, and sensing (Chen et al. 2014;

✉ Ahmed Elsayed Abouelez
a.e.abouelez@eri.sci.eg

¹ Microwave Engineering Department, Electronics Research Institute (ERI), Cairo, Egypt

² Department of Physics, School of Sciences and Engineering, The American University in Cairo, New Cairo, Egypt

Vendik and Vendik 2013; Liu and Zhang 2011). The concept of a perfect metamaterial absorber started in the early work of Landy et al. in 2008 who succeeded in making a single narrowband near-perfect absorber in a microwave band. Since this date, many designs have appeared that have perfect absorption with a single narrow band, multi-narrow band, and wideband spectrum in microwave, terahertz, infrared, and visible spectral bands (Ye et al. 2010; Bai et al. 2015; Lv et al. 2015; Liu et al. 2020; Cai et al. 2020; Chen et al. 2022; Abouelez and Abdulaleem 2023; Zolfaghary pour and Arik 2023; Errajraji et al. 2024).

The designing and manufacturing of broadband perfect absorbers for use in the mid-infrared (Mid-IR) and long-wave infrared (LWIR) bands are of high importance in several applications, including radiative cooling, thermal photovoltaic, and infrared thermal imaging.

Several designs have been presented for broadband absorbers covering the infrared range. Some of these designs are based on hyperbolic metamaterials (Huo et al. 2019) that take shapes like multilayer tapered, pyramid, and funnel (Cui et al. 2012; Liang et al. 2013; Zhou et al. 2014; Deng et al. 2018; Abdelatif et al. 2019; Yue et al. 2020). For example, an ultra-broadband infrared absorber composed of sawtoothed anisotropic metamaterial of gold and germanium is presented by Cui et al. (2012). The wavelength range of 2.5–7 μm is supported by transverse magnetic (TM) polarized light with an absorption of more than 95% at normal incidence. Additionally, this feature is adequately maintained throughout a very large range of incident angles. Since each sawtooth functions as a separate anisotropic hyperbolic metamaterial slow-light waveguide to stop and absorb incident energy, the suggested absorber can absorb light. On the same design principle, Zhou et al. (2014) experimentally realized broadband absorbers that cover the visible and infrared range based on tapered multilayered metal (Au or Al)—dielectric (Al_2O_3 , Ge, or SiO_2) structures. Structures of 9-stack (Au– Al_2O_3), 11-stack (Au–Ge), and 3-stack structure (Al– SiO_2) absorbing light from ~ 1.5 to 3 μm , ~ 2.5 to 6 μm and ~ 0.4 to 1.2 μm , respectively. Ultra-broadband absorbers based on sawtooth-like and pyramid-like metal (Al)—dielectric (ZnS) multilayer structures are proposed by Yue et al. (2020). The wavelength range of 0.2 to 15 μm is supported by the proposed absorbers. Also, based on the slow-light phenomena, an ultra-broadband absorber was designed and demonstrated in the 1–6 μm infrared wavelength region using pyramid-like multilayer waveguides composed of 13-pair Au– SiO_2 layers (Deng et al. 2018). In addition, Liang et al. (2013) proposed an ultra-broadband absorber in the wavelength range of 1–14 μm . The absorber structure is based on a pyramid-like multilayer structure composed of 15-pair Au–Ge layers. Furthermore, Abdelatif et al. (2019) proposed a broadband absorber based on funnel-shaped, cylindrical, and conical units, anisotropic metamaterial with a periodic array of (Ni/Ge) and (Ni) bottom film. With an average absorption of 96%, the suggested absorber achieves a higher absorption throughout a broad wavelength range from 0.2 to 9 μm .

Some of the materials used in the above-suggested/demonstrated absorbers may not be compatible with CMOS technology (Yue et al. 2020). On the other hand, silicon-based materials are matched with CMOS technology. Furthermore, silicon that has been doped with phosphorus (n-type Si) or boron (p-type Si) can be used in place of metal in plasmonic devices by adjusting the doping level of the silicon (Ginn et al. 2011; Zhou et al. 2015). Numerous designs have been studied numerically or experimentally in the search for doped silicon-based infrared wideband absorbers. For instance, ultra-broadband mid-IR absorbers based on low-resistivity silicon were created by Gorgulu et al. (2016). Periodically organized silicon gratings with periodicities of 7 and 8 μm offer average absorptivity of more than 90% in the wavebands of 5–18.8 μm and 5.4–20 μm , respectively. Even at large incidence angles, the structures exhibit broadband absorption performance irrespective of polarization. For the mid-IR spectral band,

Magdi et al. (2019) proposed perfect absorber structures made entirely of silicon. The structures that are suggested are made of intrinsic silicon embedded with n-doped silicon nanowires or nanoparticles. Whereas the nanowire structure exhibits a broadband absorption of more than 70% from $\lambda=5$ to 13 μm reaching up to 99% at 7 μm , the nanoparticle-based structure only produces a single broad absorption peak. Wu and Fu (2018) suggested a technique for ultra-broadband absorption in the infrared region. This technique is based on embedding an array of n-doped silicon nanowires, tilted with a specific angle relative to z-direction, in a host medium of polymethylpentene to form a metamaterial slab. Then, several slabs are stacked in the z-direction. Based on the number of slabs and the tilt angle the absorptivity bandwidth can be controlled. The absorptivity can reach 99% in the wavelength range from 2–50 μm when the number of slabs is equal to 41. This method is limited to TM polarization and, to the best of our knowledge, may be difficult to fabricate. Abdelsalam and Swillam (2022) reported a parametric study on a structure of nano prisms that are made of doped silicon (D-Si) that acts as an ultra-broadband absorber in the near and mid-infrared regions. The study shows that the proposed absorber can achieve maximum absorbed power of 92.6% of the total incident power on the absorber between 1 and 15 μm .

In this work, we present an ultra-broadband metamaterial absorber (UBMA) that covers the mid-IR and LWIR and part of Far-IR bands (i.e., wavelength range from 2.5 to ~ 22 μm) with absorptivity greater than 90% at normal incidence of electromagnetic wave. To the best of our knowledge, the design is novel and simple. The design is based on heavily D-Si, n-type doping, which acts as a metal in plasmonic devices, and silicon carbide (SiC) which is a dielectric material. Thus, the structure's materials are compatible with CMOS technology. The proposed absorber is a four-fold rotational symmetrical structure. Thus, under normal incidence, it is polarization-independent. In addition, the structure supports absorptivity greater than 80% for wide incidence angles for both transverse electric (TE) and TM polarizations.

2 Structure design, materials, and methods

The materials that are used in the proposed structure are heavily D-Si which acts as a metal and SiC which is a dielectric. The silicon is assumed to be doped with Phosphorus (n doping) with a carrier concentration of $5 \times 10^{20}/\text{cm}^3$. To calculate the relative permittivity of the D-Si in the infrared region (i.e., $\lambda > 2\mu\text{m}$), we use the Drude model which is given by

$$\epsilon(\omega) = \epsilon_{\infty} - \frac{\omega_p^2}{\omega(\omega + i\gamma)} \quad (1)$$

where ϵ_{∞} symbolizes the limiting value of the relative permittivity at high frequencies which has a value equal to 11.7 (Basu et al. 2010). ω_p (rad/s) denotes the plasma frequency which is given as a function of carrier concentration, N_e , by the following equation

$$\omega_p = \sqrt{\frac{N_e q^2}{m^* \epsilon_0}} \quad (2)$$

where the electron effective mass is taken as $m^* = 0.26m_0$, where m_0 (Kg) is the free electron mass in a vacuum. ϵ_0 (F/m) is the free-space permittivity. q (A.s) is the electron charge. The scattering rate, γ (rad/s), is given by the following equation (Basu et al. 2010)

$$\gamma = \frac{q}{m^* \mu_e} \tag{3}$$

where μ_e is the electron mobility. Electron mobility can be obtained through the measurements or by using the measurements fitting equations model. Following the fitted equation model given in (Masetti et al. 1983; Basuet al. 2010), electron mobility is calculated as a function of carrier concentration (<https://cleanroom.byu.edu/resistivitycal>). With $\epsilon_\infty = 11.7$, $\omega_p = 2.4739 \times 10^{15}$, and $\gamma = 2.0333 \times 10^{14}$, the $\epsilon(\omega)$ for the D-Si can be obtained through the Drude model. Figure 1a illustrates the real and imaginary parts of the relative permittivity of n-doped Si at the carrier concentration of $5 \times 10^{20}/\text{cm}^3$. It can be noted from the inset figure that the real part value of the relative permittivity of D-Si becomes negative for wavelengths greater than $\sim 2.7 \mu\text{m}$.

On the other hand, SiC material has several characteristics, including its excellent radiation resistance, stability at high temperatures, and high thermal conductivity (Larruquert et al. 2011). The refractive index data of the SiC is obtained from (Larruquert et al. 2011), and this data is imported to the electromagnetic simulators with the help of (ReactiveIndex.Info). Figure 1b shows fitted curves of the real and imaginary parts of the relative permittivity of the SiC using the discrete input data. From the dispersion curve shown in Fig. 1b, it can be noted that the imaginary part of the relative permittivity has a non-zero value which increases with wavelength and reaches its maximum value at wavelength around $13.5 \mu\text{m}$. Thus, it is expected that some of the absorbed power will be dissipated inside the SiC.

The proposed structure is a periodic array structure. Only one unit cell is described in detail. The unit cell has a period with a length of P in both the x and y directions. A layer of D-Si with a thickness of tm acts as a back reflector of the absorber. This thickness is high enough to ensure that the transmission is nearly zero through the back reflector. Then, to construct the first layer of the absorber, a flat dielectric layer of SiC with the thickness of $td1$ is constructed on the surface of the D-Si back reflector. After that, a square ring (SR) of D-Si (D-Si SR1) with a thickness of $tm1$ and the width of each arm, that is parallel to the x or y direction, is equal to $W1$. The inner dimension of the SR is $D \times D$. The vertical axes (A_x) shown in Fig. 2f is at a distance equal to $(D/2 + W1/2)$ form the center of the unit

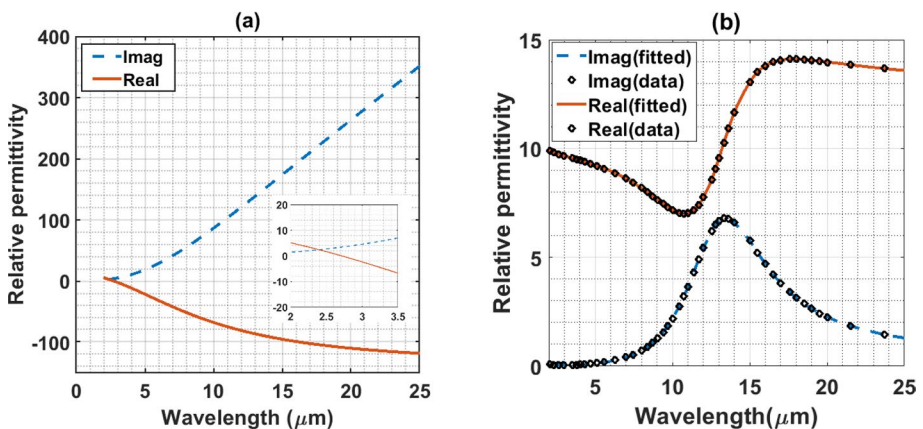


Fig. 1 Real and imaginary parts of the relative permittivity of **a** n-doped Si at carrier concentration of $5 \times 10^{20}/\text{cm}^3$. **b** SiC

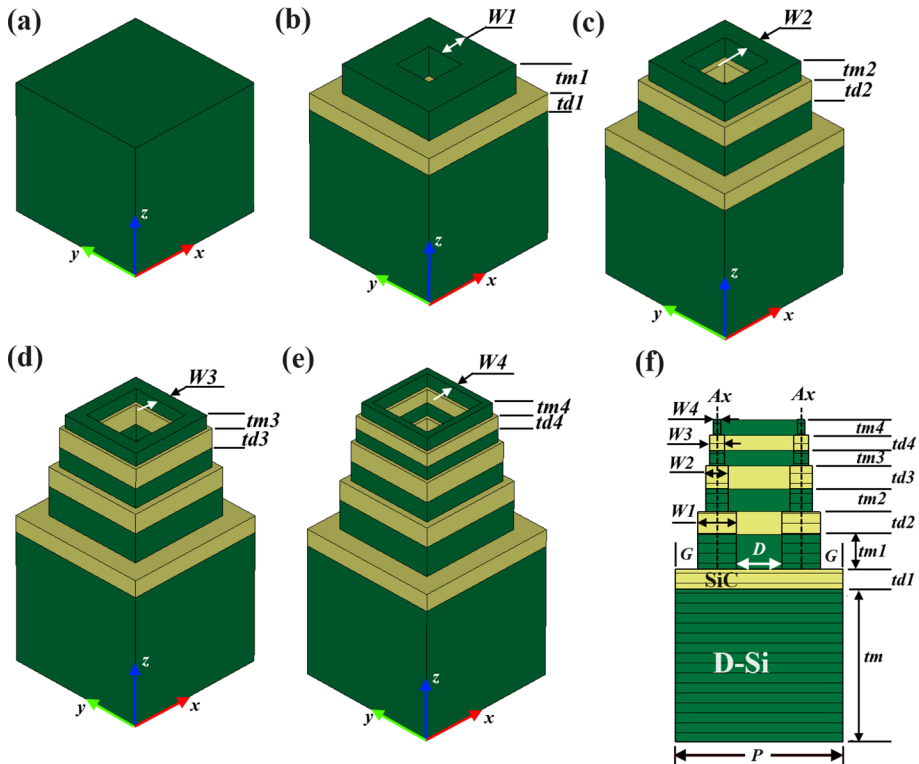


Fig. 2 The structure model of the proposed absorber. **a** D-Si back reflector. **b–e** 3D structure models in the construction direction (layer by layer). **f** Cross-section of the structure model

cell. The distance G from the edge of the SR to the edge of the unit cell is assumed to be equal to $D/2$. The second layer consists of an SR of SiC with a thickness of $td2$ and width of $W1$ followed by an SR of D-Si with a thickness of $tm2$ and width of $W2$ (D-Si SR2). The third layer consists of an SR of SiC with a thickness of $td3$ and width of $W2$ followed by an SR of D-Si with a thickness of $tm3$ and width of $W3$ (D-Si SR3). Finally, the fourth layer consists of an SR of SiC with a thickness of $td4$ and width of $W3$ followed by an SR of D-Si with a thickness of $tm4$ and width of $W4$ (D-Si SR4). All SRs have the same center and their arms are aligned around the vertical axes (A_x). The suggested fabrication process of the proposed UBMA is illustrated in the [Appendix](#).

Using a trial-and-error method, the proposed absorber structure is optimized to maintain an absorbance spectrum above 90% in the optical wavelength range of 2.5 to ~ 22 μm . Under normal incidence, the obtained absorption spectrum shown in [Fig. 3](#) is based on the following structure parameters (units in μm); $P=2.2$, $D=0.6$, $tm=2$, $td1=0.26$, $tm1=0.45$, $td2=0.3$, $tm2=0.3$, $td3=0.3$, $tm3=0.2$, $td4=0.2$, $tm4=0.2$, $W1=0.5$, $W2=0.3$, $W3=0.2$, $W4=0.1$.

To reach these optimal parameters, we used the CST Microwave Studio time-domain (TD) solver, which is based on the finite-integration method, to implement a fast parameter sweep. Then, parameter by parameter, depending on its importance, we choose the best values that enhance the absorptivity until we reach an absorbance

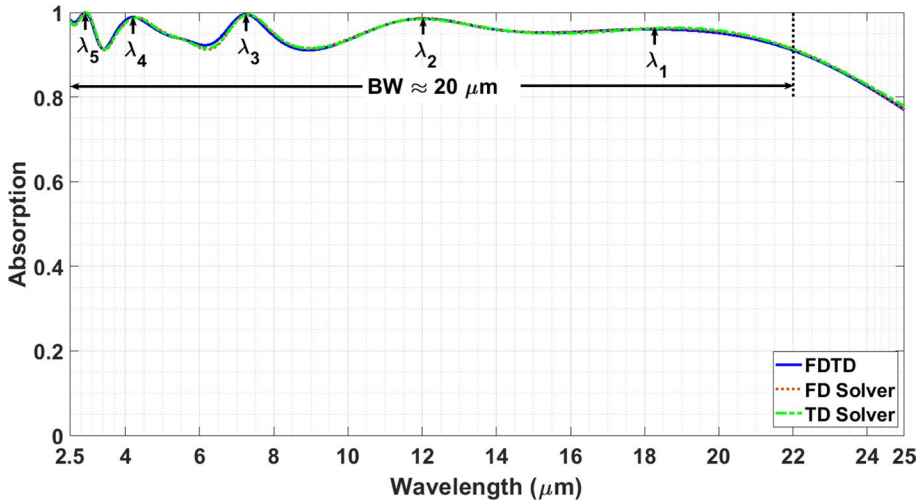


Fig. 3 Absorption spectra of the proposed absorber under normal incidence by using FDTD, TD, and FD solvers

spectrum above 90% in the optical wavelength range of 2.5 to $\sim 22 \mu\text{m}$. In addition, in all simulations, adaptive mesh refinement is activated to ensure the high accuracy of the obtained results.

The simulation of the proposed structure is, then, carried out by using the 3D finite-difference time-domain (FDTD) method with the help of the commercial software Lumerical FDTD. Due to the periodicity of the structure, only one unit cell is simulated. We set periodic boundary conditions in both the x and y directions. In the z -direction, the perfect matched layer (PML) boundary condition with the type of stretched coordinate PML is applied. The distance from the structure surface to the PML is set to be $15 \mu\text{m}$. The mesh type is chosen to be auto-non-uniform with accuracy order 4. Moreover, we used a custom meshing for the structure model with a max mesh step of $0.02 \mu\text{m}$.

In the simulation, a plane wave is applied in the negative z -direction. For normal incidence, the plane wave type is Bloch/Periodic with boundary condition setting: periodic. For non-normal incidence, the plane wave type is the Broadband Fixed Angle Source Technique (BFAST) with boundary condition setting: Bloch. The plane of incidence is the x - z plane. The electric field is parallel to the plane of incidence while the magnetic field is normal (transverse) to the plane of incidence in the case of TM-polarization. The roles of the electric field and magnetic field are exchanged for the TE-polarization case.

For verification of the FDTD simulations which were carried out by the Lumerical FDTD, we simulated the same structure model with the frequency domain (FD) solver in the CST Microwave Studio. In this solver, we apply unit cell boundary conditions in both x and y directions, open (add space) boundary conditions in the positive z -direction, and perfect electric conductor in the negative z -direction. Special meshing is taken into consideration, especially for D-Si SRs. In addition, adaptive mesh refinement is activated to ensure high accuracy of the obtained results.

3 Results and discussions

3.1 Spectral properties

The absorption spectrum, $A(\lambda)$, is computed by $A(\lambda) = 1 - T - R$ where T and R stand for the power transmission and reflection coefficients, respectively. The transmittance should be zero since the bottom D-Si layer has a thickness significantly larger than the incident beam's skin depth. As such, $A(\lambda) = 1 - R$ can be used to simplify the absorption spectrum calculation.

Figure 3 shows the absorption spectrum (in the wavelength range 2.5–25 μm) under normal incidence for TM-polarization by using the Lumerical FDTD, CST TD solver, and CST FD solver. Very good matching between the three solvers is obtained. The same result is expected in the case of TE-polarization due to the symmetry of the structure. It can be noted that the absorption is greater than 90% in the range of optical wavelengths 2.5 ~ 22 μm with an average absorption (η) of 95.23%. The average absorption is calculated with the following equation.

$$\eta = \frac{1}{\lambda_{max} - \lambda_{min}} \int_{\lambda_{min}}^{\lambda_{max}} A(\lambda) d\lambda \quad (4)$$

where, under normal incidence, $\lambda_{min} = 2.5 \mu\text{m}$ and $\lambda_{max} = 22 \mu\text{m}$ with a bandwidth of nearly 19.5 μm . Additionally, it can be observed that there are five peaks of absorption around wavelengths of $\lambda_1 = 18.275 \mu\text{m}$, $\lambda_2 = 12.0134 \mu\text{m}$, $\lambda_3 = 7.223 \mu\text{m}$, $\lambda_4 = 4.205 \mu\text{m}$, and $\lambda_5 = 2.91 \mu\text{m}$ with peak absorption of 96, 98.53, 99.53, 98.88, and 99.96%, respectively.

3.2 Field and power distributions and absorption mechanisms

To understand the physical mechanisms of the absorption corresponding to the wavelengths (starting from upper to lower wavelengths) $\lambda_1 = 18.275 \mu\text{m}$, $\lambda_2 = 12.0134 \mu\text{m}$, $\lambda_3 = 7.223 \mu\text{m}$, $\lambda_4 = 4.205 \mu\text{m}$, and $\lambda_5 = 2.91 \mu\text{m}$, the electric and magnetic field distributions of $|H_y|$, $|E_x|$, $|E_z|$, and real (E_z) components at each wavelength are calculated, by using the 3-D FDTD, considering TM-polarization and normal incidence. The effects of the addition of each layer on the overall absorption performance over the bandwidth under consideration are illustrated in Fig. 4. In Figs. 5–9, the component $|H_y|$ is plotted in the y - z cross-section (at $x=0$), while $|E_x|$, $|E_z|$, and real (E_z) components are plotted in the x - z cross-section (at $y=0$). In addition, the power loss density distribution is calculated by using the CST Microwave Studio TD solver. Figures 5–9e–h show the power loss density distribution at the outside sidewall surfaces of the structure in the x - z plane (e) and the y - z plane (g) and at the inside sidewall surfaces of the structure in the x - z cross-section (f) and the y - z cross-section (h) at the chosen wavelengths. In Figs. 5–9a–d the fields are displayed using a linear scale, whereas in Figs. 5–9e–h, for dissipated power, a log scale (normalized) is used. In addition, Fig. 10a–c shows examples of the dissipated power distributions in different conducting layers in the x - y plane while Figs. 10d and e illustrate the real (E_z) component in the x - y plane at certain D-Si SRs at the lower wavelengths (i.e., 4.205 and 2.91 μm).

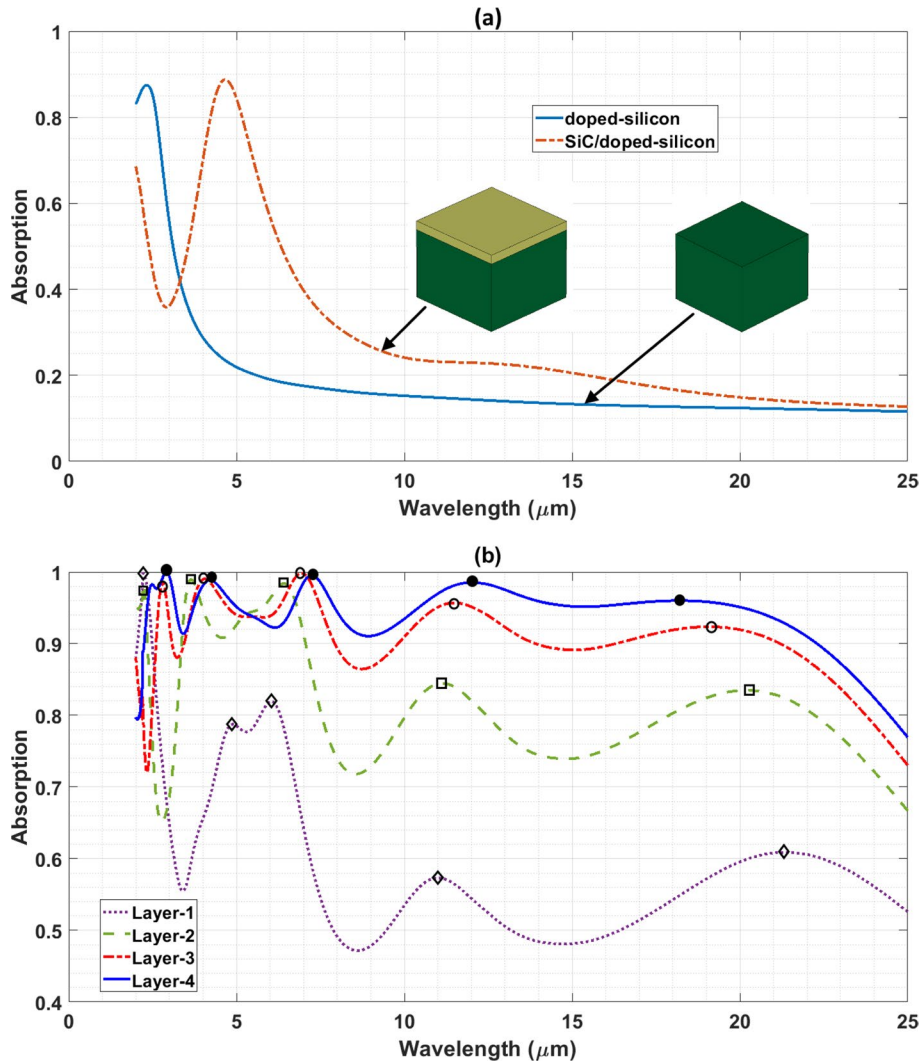


Fig. 4 Absorption spectra of the UBMA at various structural design stages. **a** For flat D-Si layer alone and flat SiC/D-Si layers. **b** For 3D structure models in the construction direction (layer by layer)

Generally, the main features of the proposed UBMA can be summarized as follows. There are four main absorption mechanisms: magnetic polariton (MP), surface plasmon polariton (SPP), localized surface plasmon resonance (LSPR), and cavity resonance (CR).

The MP mechanism is caused by the trapped magnetic field, H_y , in an insulating material (i.e., SiC) between two conducting materials (i.e., D-Si), induced by the incident magnetic field, e.g. Figure 5a, between D-Si SR1 and the D-Si back reflector and D-Si SR1 and SR2. The trapped magnetic field induces antiparallel currents in the x -direction in the two surrounding conducting layers (Zhou et al. 2006). The currents induce opposite charges at

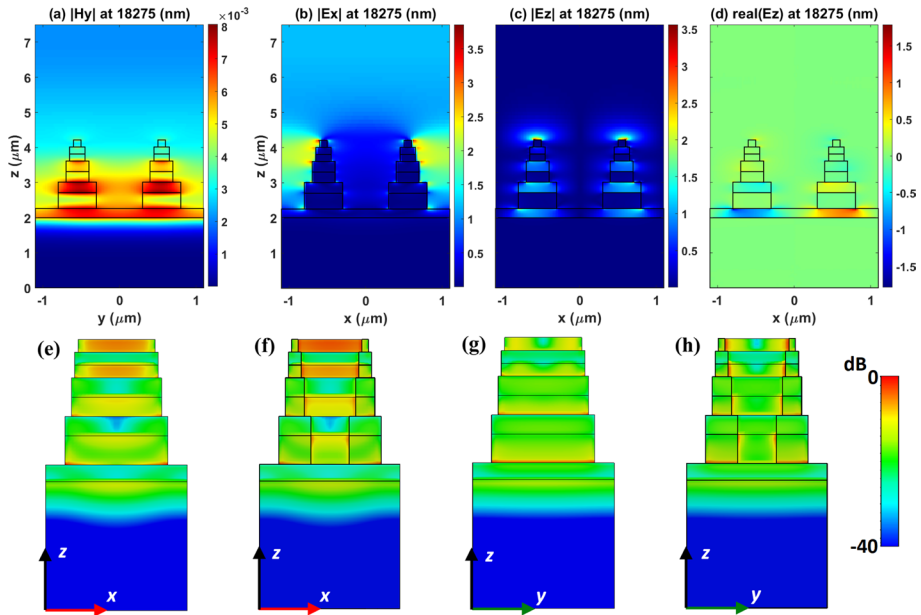


Fig. 5 Distribution of electromagnetic field components at a wavelength of 18,275 (nm). **a–c**: $|H_y|$, $|E_x|$, $|E_z|$, and **d** $\text{real}(E_z)$ components, respectively. **e–h** Power loss density distribution on the surfaces inside and outside the structure

the current ends (electric dipoles). These induced charges at the conductor's ends generate an electric field E_z in the insulating layer between the conductors, e.g. Figure 5d. The field component, E_z , causes a loss in the y -directed conducting D-Si SR arms at extreme x , caused by the imaginary part of relative permittivity, e.g. Figure 5e–h, at the bottom of the first D-Si SR1 as shown in Fig. 10a. The trapped magnetic field is accompanied by an inductance, and the polarized charges on conducting layers are accompanied by a capacitance, which together form a resonance circuit that determines mainly the resonant wavelength (Zhou et al. 2006). For the square ring pattern, a modification exists for the capacitors and inductors elements (Sakurai et al. 2014). This resonance wavelength is proportional to the length of the conductor in the x -direction but is much smaller than it (Cai et al. 2020). For instance, at 18 μm wavelength, as shown in Fig. 5, the resonance occurs in the lower layer, of nearly 2 μm length. Generally, the MP mechanism is excited mainly at the higher wavelengths (i.e., 18.275, 12.0134, and 7.223 μm).

The second mechanism is the SPP. The SPP is excited at the interface between conducting (with negative real permittivity) and insulating (with positive real permittivity) materials causing absorption (Cai et al. 2020; Qiu et al. 2021). This mechanism takes into consideration the periodic nature of the absorbing array using Floquet-diffraction modes (Zhao et al. 2013; Kim et al. 2017). This mechanism is excited, mainly, at shorter wavelengths (i.e., 4.205 and 2.91 μm), e.g. Figure 8a layers 1, 2, 3, and 4 at wavelength 4.205 μm .

The third absorption mechanism is due to LSPR, where the electric fields with opposite charges are concentrated at the edges/corners of the conducting material (i.e., D-Si) (Qiu et al. 2021), e.g., Figs. 8 and 9c, d, and Fig. 10d, e.

The fourth absorption mechanism is the CR caused by the incident electric field in the x -direction. At certain wavelengths, the field is highly concentrated in the gap between two adjacent cells (Cai et al. 2020; Qiu et al. 2021; Maruyama et al. 2001). The field, coupling adjacent cells, is seen to be stronger at gaps at certain levels whose gap dimensions are related to the resonance wavelength (i.e., as the resonance wavelength becomes shorter, the field becomes concentrated at a shorter gap) e.g., Figs. 7b and 9b.

Although the present structure is 3D, with TM-polarization excitation, other field components than E_x , E_z , and H_y are generated, e.g., E_y component (Liang et al. 2013).

Before illustrating the electromagnetic field distributions for discussing the physical mechanisms of the absorption at the peak absorption wavelengths, we will show, firstly, the effects of the addition of each layer on the overall absorption performance over the bandwidth under consideration.

Figure 4 illustrates these effects. Figure 4a shows the comparison between the spectral absorption of the flat D-Si layer and the flat SiC/D-Si layers. It can be observed that the D-Si layer alone has peak absorption around a wavelength of 2.2 μm . This absorption peak can be attributed to the free carrier absorption of the heavily D-Si with a carrier concentration of $5 \times 10^{20}/\text{cm}^3$. This absorption peak wavelength increases with decreasing doping concentration (Gorgulu et al. 2016). Due to the deposition of a SiC layer, with a thickness of $td1$, on the D-Si layer, a peak absorption is obtained around the wavelength of 4.7 μm . Thus, it is clear that the multilayered structure has a critical effect in improving spectral absorption. Figure 4b displays the effect of adding layer by layer to the structure in the growth direction. The addition of layer-1 results in an absorption spectrum with five peaks (labeled by \diamond) at wavelengths, arranged from higher wavelength to lower wavelength, around (21.5, 11, 6, 4.86, and 2.3 μm). These peak absorption wavelengths are expected to be generated due to the excitation of one or more absorption mechanisms (i.e., MP, SPP, or LSPR), as will be discussed in detail for each of the peak absorption wavelengths, or due to the free carrier absorption of the D-Si SR (i.e., corresponding to the wavelength of 2.3 μm). After adding the second layer, the absorption is enhanced and the peaks are slightly shifted with respect to those generated by the first layer alone (labeled by \square) (i.e., 20.3, 11.15, 6.4, 3.6, and 2.24 μm). These shifts in the wavelength are expected to be a result of the coupling between the excited mechanisms due to the first layer and those excited due to the addition of the second layer. The third layer made extra enhancement with a shift in absorption peaks (labeled by \circ). However, the average absorption is less than 90%. The addition of a fourth layer made the absorption greater than 90% over a bandwidth of nearly 19.5 μm .

In the following, we will investigate and analyze, at the different wavelengths with absorption peaks, the relative contributions of each mechanism and their impact on the absorber's performance.

Figure 5 shows the electromagnetic field distributions and power loss density at the wavelength of 18.275 μm . At this wavelength, it can be noted from Fig. 5a that the magnetic field component $|H_y|$ is highly concentrated inside the flat SiC layer between the first D-Si SR and D-Si back reflector and inside the SiC SR layer inserted between the first and second D-Si SRs. This magnetic field distribution indicates the excitation of MPs. Additionally, a weak magnetic field can be observed to be concentrated between the second and third D-Si SRs which, also indicates an excitation of moderate MP. These magnetic polaritons are expected to be the main reason for the high absorption around the wavelength of 18 μm . The blue shift of the peak wavelengths (from 21.5 to \sim 18 μm) due to the addition of the layers shown in Fig. 4b can be attributed to the coupling of these MPs.

On the other hand, the electric field component $|E_z|$, as shown in Fig. 5c, is concentrated in the insulating SiC, especially at the y-directed SRs arms at extremes of x-direction, and between the top D-Si SR and the air. For more clarification, Fig. 5d displays the $\text{real}(E_z)$ component of the electric field distribution, where the electric dipole formed at the interface between the D-Si SRs and the SiC results in the generation of E_z field with opposite directions at the extreme parts in the x-direction. The previous description is confirmed by the power loss distribution. Figure 5g and h show that the power is dissipated, mainly, in the lower sides of the first and second D-Si SRs along the arms parallel to the y-direction at the extremes in the x-direction, i.e. at the outer edges, Fig. 5e and f. The dissipation distribution in these layers changes with z due to the presence of MPs above and below the layer. Moreover, concerning the upper layers (i.e., layers 3 and 4), it can be noted from Fig. 5b that a moderate electric field, E_x , is concentrated at the gap between adjacent unit cells, especially at the top sidewall edges of structure layers. This field also contributes to enhancing the absorption at the wavelength under consideration. The corresponding power loss in layers 3 and 4 is shown in Fig. 5e–h to be in the arms along the x-direction. Also, it can be noted that there is some moderate power dissipated in the SiC layers and in the D-Si back reflector which can be attributed to the internal losses of D-Si and SiC material (see Fig. 1).

Figure 6 displays the electromagnetic field and power loss density distributions at the wavelength of 12.04 μm . It can be noted from Fig. 6a that a weak and moderate magnetic field is concentrated inside the flat SiC layer between the first D-Si SR and D-Si back reflector and inside the SiC SR layer inserted between the first and second D-Si SRs, respectively. This indicates the excitation of weak and moderate MPs compared to that excited at

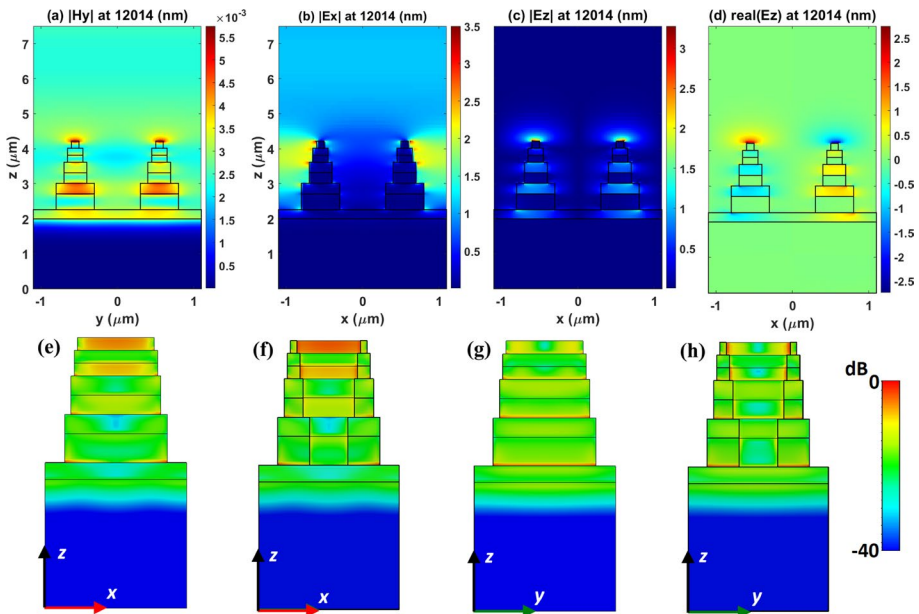


Fig. 6 Distribution of electromagnetic field components at a wavelength of 12,014 (nm). **a–c:** $|H_y|$, $|E_x|$, $|E_z|$, and **d** $\text{real}(E_z)$ components, respectively. **e–h** Power loss density distribution on the surfaces inside and outside the structure

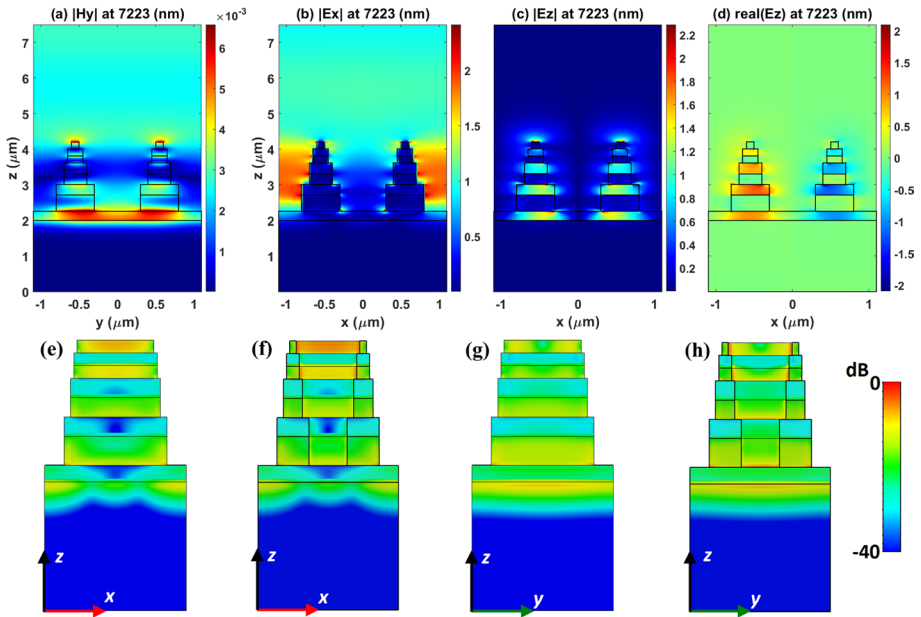


Fig. 7 Distribution of electromagnetic field components at a wavelength of 7223 (nm). **a–c:** $|H_y|$, $|E_x|$, $|E_z|$, and **d** $\text{real}(E_z)$ components, respectively. **e–h** Power loss density distribution on the surfaces inside and outside the structure

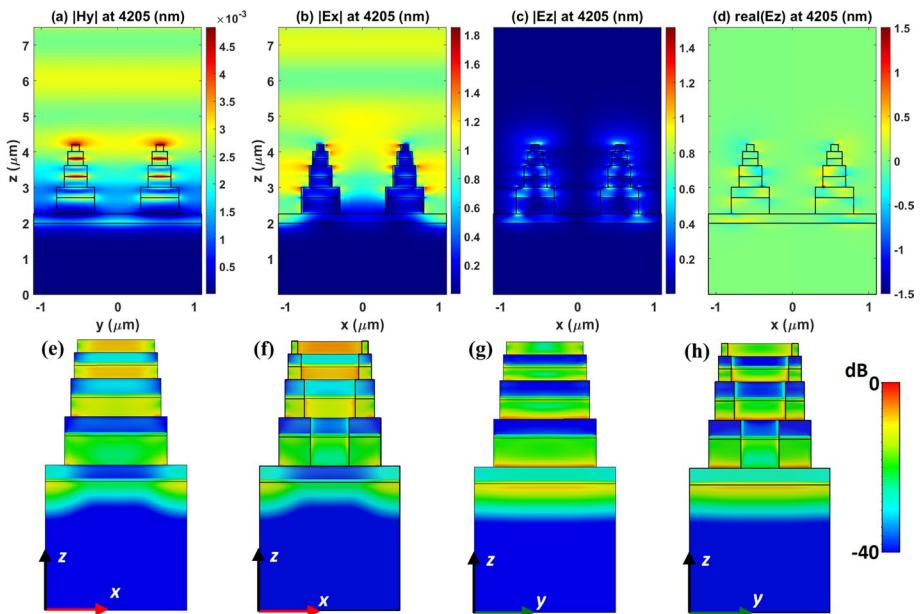


Fig. 8 Distribution of electromagnetic field components at a wavelength of 4205 (nm). **a–c:** $|H_y|$, $|E_x|$, $|E_z|$, and **d** $\text{real}(E_z)$ components, respectively. **e–h** Power loss density distribution on the surfaces inside and outside the structure

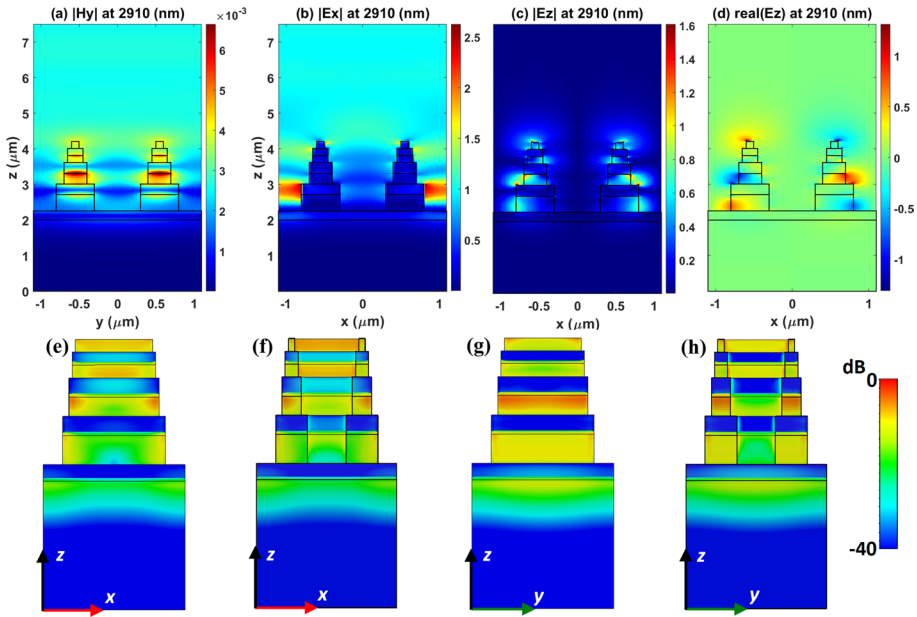


Fig. 9 Distribution of electromagnetic field components at a wavelength of 2910 (nm). **a–c:** $|H_y|$, $|E_x|$, $|E_z|$, and **d** real(E_z) components, respectively. **e–h** Power loss density distribution on the surfaces inside and outside the structure

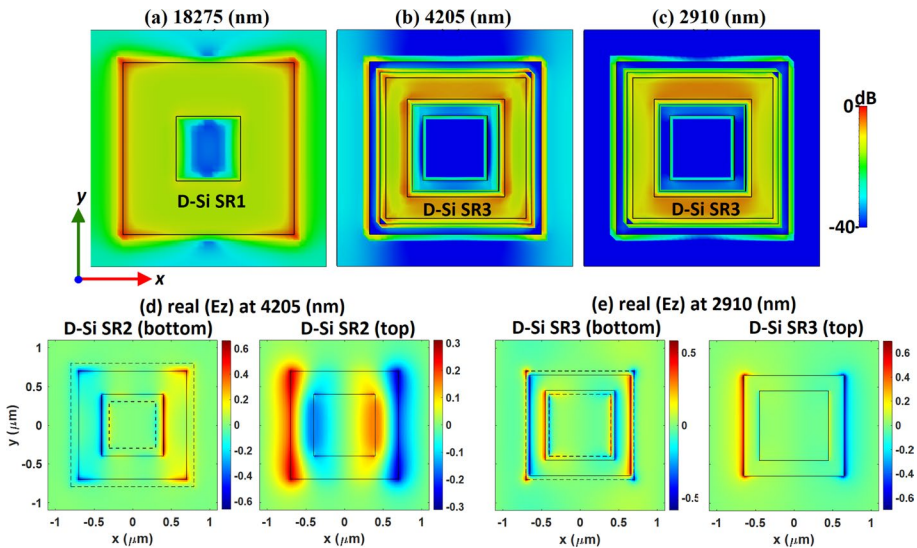


Fig. 10 Power loss density distributions in the x–y plane for **a** D-Si SR1 at 18.275 μm , **b** D-Si SR3 at 4.205 μm , and **c** D-Si SR3 at 2.91 μm . Real(E_z) component distribution in the x–y plane for **d** D-Si SR2 bottom and top surfaces at 4.205 μm and **e** D-Si SR3 bottom and top surfaces at 2.91 μm

the wavelength of 18.275 μm at the same layers. Also, it can be noted from Fig. 6a, c, and d that the magnetic and electric fields are concentrated at the interface between the upper surface of the fourth D-Si SR and the air which indicates an excitation of SPP. Thus, the absorption at the wavelength of 12.04 μm is enhanced, mainly, by the moderate MP and the SPP absorption mechanisms. In addition, the moderate electric field, E_x , is concentrated at the air gap between adjacent unit cells especially at the edges of structure layers (like that shown in Fig. 5b) which contributes to enhancing the absorption. Moreover, the distribution of power loss density, shown in Fig. 6e–h, in general, has the same distribution shown in Fig. 5e–h, however, there is a slightly higher power loss than the power loss at the wavelength of 18.275 μm .

At the wavelength of 7.223 μm , considering layer 1, Fig. 7a shows that the magnetic field is enhanced, mainly, in the flat SiC layer between the first D-Si SR and D-Si back reflector. This indicates an excitation of MP. Considering layers 2 and 3, it can be noted, from Fig. 7b, that the electric field component, $|E_x|$, is highly confined in the air gap between the adjacent cells. This indicates an excitation of CR. Also, $|E_x|$ is moderately confined in the flat SiC layer between the adjacent cells. This is accompanied by the power dissipated in the D-Si back reflector concentrated in the region between adjacent cells along the y-direction as indicated in Fig. 7e and f. In addition, considering layer 4, it can be noted from Fig. 7a, c, and d that the magnetic and electric fields are concentrated at the interface between the upper surface of the fourth D-Si SR and the air which indicates an excitation of SPP. These electromagnetic field distributions indicate that the absorption at the wavelength of 7.223 μm is enhanced, mainly, by the MP, CR, and SPP absorption mechanisms. Additionally, Figs. 7c and d indicate high electric field confinement inside the SiC flat layer and SiC SRs especially at the inner edges of SRs. Moreover, Fig. 7e–h illustrates the power loss density at this wavelength. It can be noted that the power is dissipated in D-Si SRs 3 and 4 at the arms parallel to the x-direction and D-Si SRs 1 and 2 at the lower side interface along the arms parallel to the y-direction. Also, the power is dissipated in the inside corners of the D-Si SRs. In addition, the noted power dissipation inside the SiC at the higher wavelengths (i.e., 18.275 and 12.04 μm) becomes lower at this wavelength due to the lower value of the imaginary part of the relative permittivity of the SiC.

At the wavelength of 4.205 μm , Fig. 8a indicates that the magnetic field is confined at the interfaces between D-Si and SiC SRs and the interface between the upper D-Si SR and the air. These field distributions indicate an excitation of SPPs. The confinement of these fields is gradually increasing from lower to upper layers. Furthermore, it is evident from Fig. 8a and b that the electromagnetic fields (i.e., $|E_x|$ and $|H_y|$) concentrate above the structure and extend far from its surface with distributions that have a standing wave profile (Cai, et al. 2020). Figure 8b illustrates that there is a moderate confinement of the electric field component, $|E_x|$, inside the SRs, inside the air gap between the adjacent cells, and moderate confinement in the flat SiC layer between the adjacent cells. In addition, Fig. 8c and d show the distribution of the z-component of the electric field which indicates the localization of the electric field at the edges of D-Si SRs. This localization of the electric field is clarified in Fig. 10d which shows the distribution of real (E_z) in the x–y plane at the bottom and top interfaces of D-Si SR2. It can be noted that the field is localized at the edges and the corners of the D-Si SR with opposite polarities. These field distributions indicate an excitation of LSPR. Thus, it can be indicated that the absorption at the wavelength of 4.205 μm is enhanced, mainly, by the SPP and LSPR mechanisms. Moreover, it can be noted from Fig. 8e and f that power is highly dissipated in D-Si SRs 2, 3, and 4 in the arms parallel to the y-direction and inside corners. In Fig. 10b, for the D-Si SR3, the power is

highly dissipated, mainly, in the arms parallel to the x-direction and inside corners. From Fig. 8g and h, it can be noted that power is highly dissipated in D-Si SRs 1 and 2 at the lower sides of D-Si SRs in the arms parallel to the x-direction. In addition, the power dissipated in the doped-Si back reflector is concentrated in the region between adjacent cells along the y-direction. Furthermore, the dissipated power inside the SiC becomes insignificant, especially in SiC SRs, due to the low losses at that wavelength.

Finally, at the wavelength of 2.9 μm , considering layer 1, Fig. 9b shows strong confinement of the electric field component, $|E_x|$, inside the air gap between the adjacent cells at this layer. This can be attributed to the excitation of CR. Considering layers 1, 2, 3, and 4, Fig. 9a indicates magnetic field confinement at the interfaces between D-Si and SiC SRs. This magnetic field confinement is weak at the interface between the first D-Si SR and the upper SiC SR, then becomes stronger at the higher interfaces between D-Si and SiC SRs, especially between the second D-Si SR and the upper SiC SR. These field distributions indicate an excitation of SPP. Also, it is clear, from Fig. 9c and d, that the z-component is localized at the outer sidewall edges of the D-Si SRs. The localization of the electric field is clarified in Figs. 9d and 10e which show the distribution of real (E_z) in the x-y plane at the bottom and top interfaces of D-Si SR. It can be noted that the field is localized at the edges and the corners of the D-Si SR with opposite polarities. These field distributions indicate an excitation of LSPR. Thus, it can be indicated that the absorption at the wavelength of 2.9 μm is enhanced, mainly, by the CR, SPR, and LSPR absorption mechanisms. These notes are supported by the dissipated power distribution shown in Fig. 9e-h and Fig. 10c. It can be noted that the power is highly dissipated in all doped-Si SRs especially the second D-Si SR in addition to some power that is dissipated in the D-Si back reflector.

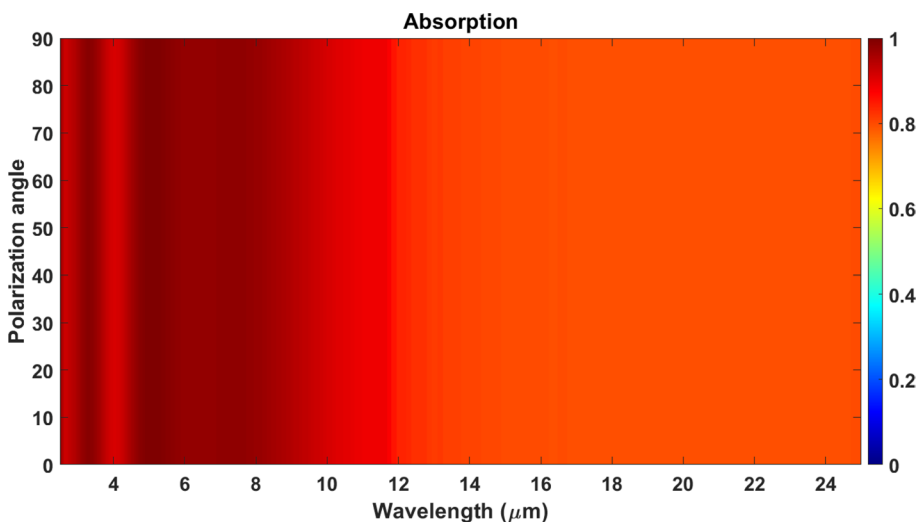


Fig. 11 Absorption spectra at normal incidence calculated against the polarization angle

3.3 Impact of polarization and oblique incidence

Due to the symmetric property of the proposed absorber, it is expected that there will be no variation in the absorption spectrum due to the variation of polarization angle (i.e., the angle between the projection of the electric field and the x-direction). Figure 11 shows the absorption spectrum as a function of polarization angle (degree) at normal incidence. It can be noted that there is no variation in the absorption spectrum due to the variation of the polarization angle.

On the other hand, we discussed, in the previous subsection, the physical mechanisms of the excited resonances that enhance the absorption at certain wavelengths. These

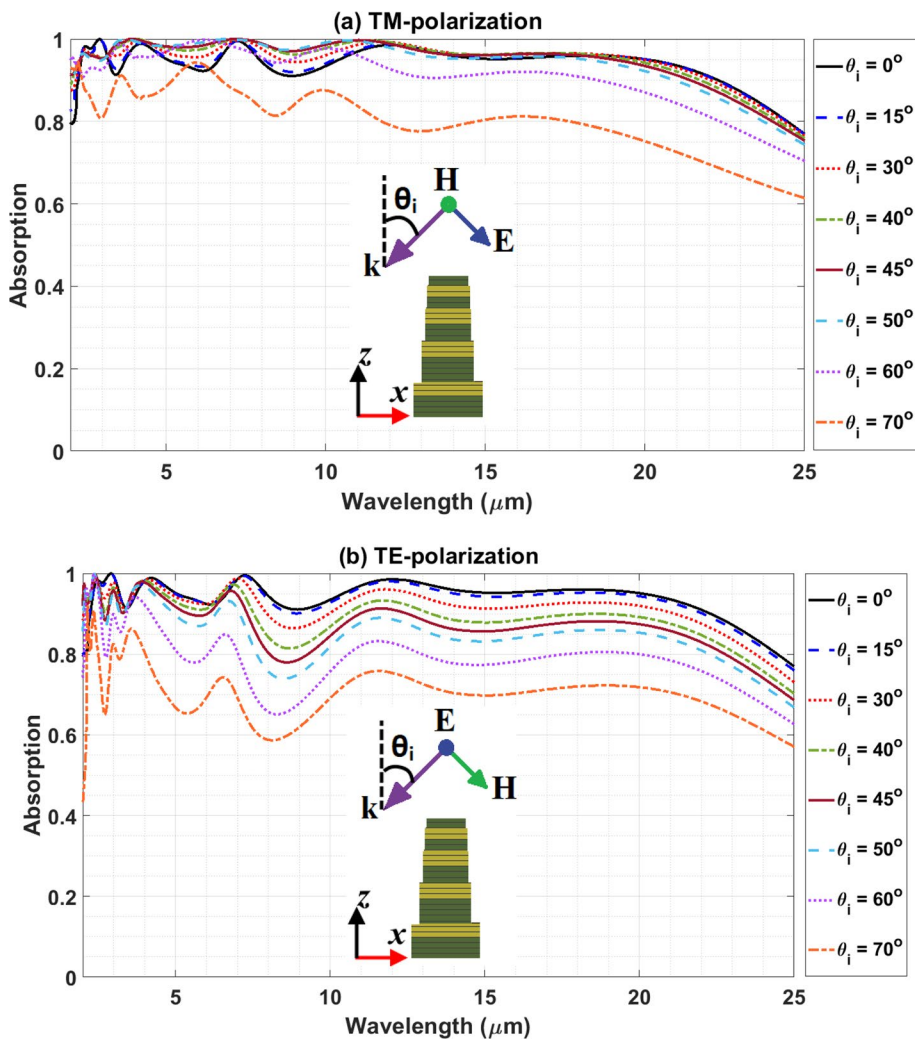


Fig. 12 The proposed UBMA’s absorption spectra for **a** TM polarization and **b** TE polarization at various incidence angles

Table 1 Average absorption of the proposed UBMA at different incident angles for TM polarization (η_{TM}) and TE polarization (η_{TE})

θ_i	0°	15°	30°	40°	45°	50°	60°	70°
$\eta_{TM}(\%) \cong$	95.23	95.57	96.32	96.73	96.66	96.19	92.79	81.91
$\eta_{TE}(\%) \cong$	95.23	94.65	92.53	89.75	87.8	85.4	79	70.6

resonances may be excited by electric field or magnetic field components. At the normal incidence of the plane wave, the proposed absorber has the same performance for both TE and TM polarizations where the structure has the symmetrical property. However, although this symmetrical property of the structure, it is expected that oblique incidence of TE and TM polarized waves will give different performances. To examine these effects on the performance of the proposed absorber, the absorption spectrum is computed at different incidence angles, θ_i , under TE and TM polarizations. The incidence angle, θ_i , concerning the wave vector, \mathbf{k} , is shown in the inset figures in Fig. 12a and b for TE and TM polarizations, respectively. Figure 12a shows the absorption spectrum of the proposed absorber at different incidence angles under TM polarization. The average absorption, η_{TM} , is calculated at each incidence angle and tabulated in Table 1. Obviously, the absorber has an average absorption greater than 90% for incidence angles up to 60° and average absorption greater than 80% for incidence angles up to 70°. Also, it can be noted that the values of the average absorption for θ_i greater than 0° up to 50° are higher than that corresponding to $\theta_i = 0^\circ$. This can be attributed to the blueshift of the absorption peaks, especially the higher resonant wavelengths (i.e., $\lambda \cong 18, 12,$ and $7 \mu\text{m}$), and the broadening around the peaks between each other as illustrated in Fig. 12(a). The blueshift is usually caused by the resonance caused, mainly, by MP (Ye et al. 2010; Bai et al. 2015) at TM polarization under oblique incidence where the MP is caused by the H_y component of the magnetic field (Ye et al. 2010). The broadening can be attributed to the interaction with a large area of the lossy materials (i.e., D-Si and SiC).

The proposed absorber's absorption spectrum under TE polarization is displayed in Fig. 12b at various incidence angles. At each incidence angle, the average absorption, η_{TE} , is computed and given in Table 1. It can be observed that the absorption amplitude and the η_{TE} decrease as the incidence angle increases especially at higher peak wavelengths (i.e., $\lambda \cong 18, 12,$ and $7 \mu\text{m}$). This is because the MPs, under TE polarization, are excited by the H_x component of the incident field. Under TE polarization, the proposed absorber can achieve average absorptivity greater than 80% for incidence angles up to 50°. In addition, the absorption spectrum of the normal incidence is nearly overlapped with those of incident angles up to $\theta_i = 30^\circ$ and the average absorption is greater than 90%.

3.4 Comparison study

In this subsection, the performance of the proposed UBMA is compared to some of the reported designs in infrared broadband absorbers. The comparison is based on, namely, the structure shape, materials type, wavelength range, value of absorption at normal incidence, techniques of verification, wide-incident angle absorption capability, and polarization sensitivity as presented in Table 2.

Table 2 Comparison of the proposed UBMA with some reported infrared broadband absorbers

References	Structure and materials	Wavelength range	Absorption (normal incidence)	Verification techniques	Polarization sensitivity	Absorption with wide-incident angle
Gorgultu et al. (2016)	Silicon gratings of (D-Si/SiO ₂) with periodicities of 7 μm and 8 μm	5–18.8 μm for P = 7 and 5.4–20 μm for P = 8 μm	> 90%	Simulation	In insensitive	yes
Deng et al. 2018	Pyramid-like 13-pair Au-SiO ₂ layers	1–6 μm	> 90%	Simulation	In insensitive	NA
Magdi et al. (2019)	Intrinsic silicon embedded with n-doped silicon nanowires or nanoparticles	5 to 13 μm for the nanowire structure	more than 70%	Simulation	NA	yes
Wu and Fu (2018)	Stacked slabs of Polymethylpentene embedded with tilted n-doped silicon nanowires	2–50 μm when the number of slabs is equal to 41	99%	Simulation	Sensitive	yes
Abdelsalam and Swillam (2022)	Funnel-shaped, cylindrical, and conical units of nickel-germanium (Ni/Ge) and (Ni) bottom film	0.2 to 9 μm	> 90%	Simulation	In insensitive	yes
This work	Nano prisms of D-Si and intrinsic silicon Multilayer of square rings of D-Si and SiC	1 to 15 μm 2.5 to 22 μm	> 90% > 90%	Simulation Simulation	Sensitive In insensitive	NA yes

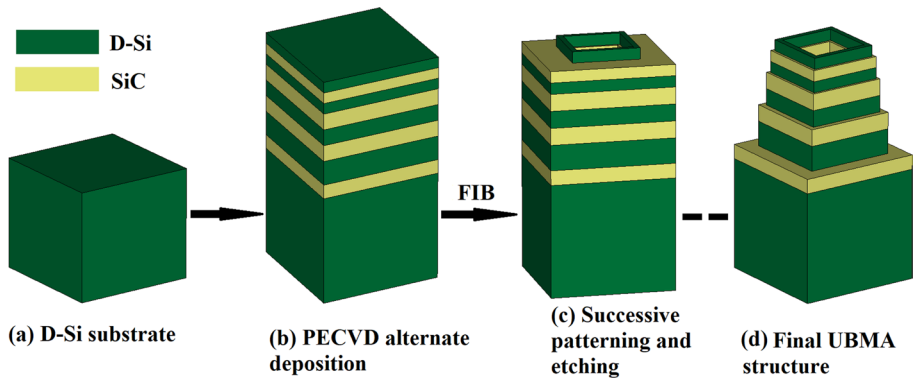


Fig. 13 The fabrication steps of the proposed UBMA.

4 Conclusion

In summary, a novel design of a UBMA is proposed and numerically investigated using the 3D-FDTD method. The proposed structure is a periodic array structure consisting of multilayer square rings of D-Si and SiC mounted on SiC/D-Si film. Under normal incidence of light wave, this UBMA achieved absorption greater than 90% from 2.5 to 22 μm with an average absorption of 95%. The absorber is polarization-insensitive because of its perfect symmetry. Additionally, the TM and TE modes' absorption of the UBMA at oblique incidence is examined. For TM-polarization, the average absorption is greater than 80% for incidence angles up to 70° while for TE-polarization, the average absorption is greater than 80% for incidence angles up to 50°. The comprehensive analysis of the electromagnetic field distributions at different wavelengths in the absorption band attributes the enhanced absorptivity to the excitation of MP, SPP, LSPR, and CR.

Appendix (Proposed fabrication process)

In this Appendix, we will illustrate a suggestion for the fabrication process. At first, the heavily D-Si substrate that acts as a back reflector is prepared as shown in Fig. 13a. The plasma-enhanced chemical vapor deposition (PECVD) can be used to deposit 4-pair of SiC/D-Si layers on a heavily D-Si substrate as shown in Fig. 13b (Kuo 1997; Seo et al. 2002). During the PECVD process, Si can be doped (Kuo 1997). Perfect control of the thickness of each layer can be achieved by adjusting the process settings such as temperature and deposition time. The D-Si/SiC SRs' patterned multilayer can be created with a Focused Ion Beam (FIB) system (Deng et al. 2018). As shown in Fig. 13c, successive patterning and etching of D-Si/SiC layers can be implemented by adjusting the ion beam milling dwell time at various milling depths along the side walls of the D-Si/SiC SRs until we reach the final UBMA structure shown in Fig. 13d (Deng et al. 2018; Chekurov et al. 2010; Reyntjens and Puers 2001; Menzel et al. 1998).

Author contributions A.E.A: Conceptualization, Formal analysis, Investigation, Methodology, Validation, Visualization, Writing—original draft and Writing—review & editing. E.A.E.: Validation, Investigation,

and Writing—review & editing. M. S.: The idea of using heavily doped silicon as a metal and its related discussions. All authors read and approved the final manuscript.

Funding Open access funding provided by The Science, Technology & Innovation Funding Authority (STDF) in cooperation with The Egyptian Knowledge Bank (EKB). Funding does not apply to this article (no funds for this research).

Data availability The datasets used and/or analyzed during the current study are available from the corresponding author upon reasonable request.

Declarations

Conflict of interest We declare that the authors have no competing interests.

Ethical approval Fortunately, there are no ethical concerns associated with this work.

Open Access This article is licensed under a Creative Commons Attribution 4.0 International License, which permits use, sharing, adaptation, distribution and reproduction in any medium or format, as long as you give appropriate credit to the original author(s) and the source, provide a link to the Creative Commons licence, and indicate if changes were made. The images or other third party material in this article are included in the article's Creative Commons licence, unless indicated otherwise in a credit line to the material. If material is not included in the article's Creative Commons licence and your intended use is not permitted by statutory regulation or exceeds the permitted use, you will need to obtain permission directly from the copyright holder. To view a copy of this licence, visit <http://creativecommons.org/licenses/by/4.0/>.

References

- Abdelatif, G.Y., Hameed, M.F.O., Obayya, S.S.A., Hussein, M.: Ultrabroadband absorber based on a funnel-shaped anisotropic metamaterial. *JOSA B* **36**(10), 2889–2895 (2019)
- Abdelsalam, M., Swillam, M.A.: Ultra-broadband MIR super absorber using all silicon metasurface of triangular doped nanoprisms. *Sci. Rep.* **12**(1), 14802 (2022)
- Abouelez, A.E., Abdulaleem, M.N.: Design and analysis of quad-band polarization-insensitive infrared perfect metamaterial absorber with a wide-incident angle. *Opt. Quant. Electron.* **55**, 1045 (2023)
- Bai, Y., Zhao, L., Ju, D., Jiang, Y., Liu, L.: Wide-angle, polarization-independent and dual-band infrared perfect absorber based on L-shaped metamaterial. *Opt. Express* **23**(7), 8670–8680 (2015)
- Basu, S., Lee, B.J., Zhang, Z.M.: Infrared radiative properties of heavily doped silicon at room temperature. *J. Heat Transf.* **132**(2), 023301(2010). <https://doi.org/10.1115/1.4000171>
- Cai, H., Sun, Y., Wang, X., Zhan, S.: Design of an ultra-broadband near-perfect bilayer grating metamaterial absorber based on genetic algorithm. *Opt. Express* **28**(10), 15347–15359 (2020)
- Chekurov, N., Grigoros, K., Sainiemi, L., Peltonen, A., Tittonen, I., Franssila, S.: Dry fabrication of micro-devices by the combination of focused ion beam and cryogenic deep reactive ion etching. *J. Micro-mech. Microeng.* **20**(8), 085009 (2010)
- Chen, Z., Guo, B., Yang, Y., Cheng, C.: Metamaterials-based enhanced energy harvesting: a review. *Physica B: Condensed Matter* **438**, 1–8 (2014)
- Chen, C., Liu, Y., Jiang, Z.Y., Shen, C., Zhang, Y., Zhong, F., Chen, L., Zhu, S., Liu, H.: Large-area long-wave infrared broadband all-dielectric metasurface absorber based on maskless laser direct writing lithography. *Opt. Express* **30**(8), 13391–13403 (2022)
- Cui, Y., Fung, K.H., Xu, J., Ma, H., Jin, Y., He, S., Fang, N.X.: Ultrabroadband light absorption by a sawtooth anisotropic metamaterial slab. *Nano Lett.* **12**(3), 1443–1447 (2012)
- Deng, H., Mathai, C.J., Gangopadhyay, S., Gao, J., Yang, X.: Ultra-broadband infrared absorption by tapered hyperbolic multilayer waveguides. *Opt. Express* **26**(5), 6360–6370 (2018)
- Errajraji, K., Jebbor, N., Das, S., Islam, T., Madhav, B.T.P., El-Arrouch, T.: Design and analysis of a multi-band miniaturized metamaterial absorber for wireless communication applications. *Opt. Quant. Electron.* **56**(2), 232 (2024)
- Ginn, J.C., Jarecki, R.L., Shaner, E.A., Davids, P.S.: Infrared plasmons on heavily-doped silicon. *J. Appl. Phys.* **110**(4), 043110 (2011)

- Gorgulu, K., Gok, A., Yilmaz, M., Topalli, K., Bıyıklı, N., Okyay, A.K.: All-silicon ultra-broadband infrared light absorbers. *Sci. Rep.* **6**(1), 38589 (2016)
- Huo, P., Zhang, S., Liang, Y., Lu, Y., Xu, T.: Hyperbolic metamaterials and metasurfaces: fundamentals and applications. *Adv. Opt. Mater.* **7**(14), 1801616 (2019)
- Kim, J., Han, K., Hahn, J.W.: Selective dual-band metamaterial perfect absorber for infrared stealth technology. *Sci. Rep.* **7**(1), 1–9 (2017)
- Kuo, Y.: Doping gas effects on plasma enhanced chemical vapor deposition on heavily phosphorus-doped n^+ silicon film. *Appl. Phys. Lett.* **71**(19), 2821–2823 (1997)
- Landy, N.I., Sajuyigbe, S., Mock, J.J., Smith, D.R., Padilla, W.J.: Perfect metamaterial absorber. *Phys. Rev. Lett.* **100**(20), 207402 (2008)
- Larruquert, J.I., Pérez-Marín, A.P., García-Cortés, S., Rodríguez-de Marcos, L., Aznárez, J.A., Méndez, J.A.: Self-consistent optical constants of SiC thin films. *JOSA A* **28**(11), 2340–2345 (2011)
- Liang, Q., Wang, T., Lu, Z., Sun, Q., Fu, Y., Yu, W.: Metamaterial-based two dimensional plasmonic sub-wavelength structures offer the broadest waveband light harvesting. *Adv. Opt. Mater.* **1**(1), 43–49 (2013)
- Liu, Y., Zhang, X.: Metamaterials: a new frontier of science and technology. *Chem. Soc. Rev.* **40**(5), 2494–2507 (2011)
- Liu, Y., Liu, H., Jin, Y., Zhu, L.: Ultra-broadband perfect absorber utilizing a multi-size rectangular structure in the UV-MIR range. *Results Phys.* **18**, 103336 (2020)
- Lv, J., Yuan, R.-y., Song, X., Yan, H.: Broadband polarization-insensitive terahertz absorber based on heavily doped silicon surface relief structures. *J. Appl. Phys.* **117**(1), (2015). <https://doi.org/10.1063/1.4905386>
- Magdi, S., El-Diwany, F., Swillam, M.A.: Broadband MIR harvester using silicon nanostructures. *Sci. Rep.* **9**(1), 5829 (2019). <https://doi.org/10.1038/s41598-019-42022-2>
- Maruyama, S., Kashiwa, T., Yugami, H., Esashi, M.: Thermal radiation from two-dimensionally confined modes in microcavities. *Appl. Phys. Lett.* **79**(9), 1393–1395 (2001)
- Masetti, G., Severi, M., Solmi, S.: Modeling of carrier mobility against carrier concentration in arsenic-, phosphorus-, and boron-doped silicon. *IEEE Trans. Electron Devices* **30**(7), 764–769 (1983)
- Menzel, R., Bachmann, T., Machalet, F., Wesch, W., Lang, U., Wendt, M., Musil, C., Mühle, R.: Surface smoothing and patterning of SiC by focused ion beams. *Appl. Surf. Sci.* **136**(1–2), 1–7 (1998)
- Qiu, Y., Zhang, P., Li, Q., Zhang, Y., Li, W.: A perfect selective metamaterial absorber for high-temperature solar energy harvesting. *Sol. Energy* **230**, 1165–1174 (2021)
- ReactiveIndex.Info: <https://refractiveindex.info/?shelf=main&book=SiC&page=Larruquert> (accessed on 22 Feb 2024)
- Reyntjens, S., Puers, R.: A review of focused ion beam applications in microsystem technology. *J. Micro-mech. Microeng.* **11**(4), 287 (2001)
- Sakurai, A., Zhao, B. and Zhang, Z.M.: Prediction of the resonance condition of metamaterial emitters and absorbers using LC circuit model. In *International Heat Transfer Conference Digital Library*. Begel House Inc. (2014)
- Seo, J.Y., Yoon, S.Y., Nihara, K., Kim, K.H.: Growth and microhardness of SiC films by plasma-enhanced chemical vapor deposition. *Thin Solid Films* **406**(1–2), 138–144 (2002)
- Vendik, I.B., Vendik, O.G.: Metamaterials and their application in microwaves: a review. *Tech. Phys.* **58**(1), 1–24 (2013)
- Wu, X., Fu, C.: Ultra-broadband perfect absorption with stacked asymmetric hyperbolic metamaterial slabs. *Nanoscale Microscale Thermophys. Eng.* **22**(2), 114–123 (2018)
- Ye, Y.Q., Jin, Y., He, S.: Omnidirectional, polarization-insensitive and broadband thin absorber in the terahertz regime. *JOSA B* **27**(3), 498–504 (2010)
- Yue, S., Hou, M., Wang, R., Guo, H., Hou, Y., Li, M., Zhang, Z., Wang, Y., Zhang, Z.: Ultra-broadband metamaterial absorber from ultraviolet to long-wave infrared based on CMOS-compatible materials. *Opt. Express* **28**(21), 31844–31861 (2020)
- Zhao, B., Wang, L., Shuai, Y., Zhang, Z.M.: Thermophotovoltaic emitters based on a two-dimensional grating/thin-film nanostructure. *Int. J. Heat Mass Transf.* **67**, 637–645 (2013)
- Zhou, J., Economon, E.N., Koschny, T., Soukoulis, C.M.: Unifying approach to left-handed material design. *Opt. Lett.* **31**(24), 3620–3622 (2006)
- Zhou, J., Kaplan, A.F., Chen, L., Guo, L.J.: Experiment and theory of the broadband absorption by a tapered hyperbolic metamaterial array. *ACS Photonics* **1**(7), 618–624 (2014)
- Zhou, S., Pi, X., Ni, Z., Ding, Y., Jiang, Y., Jin, C., Delerue, C., Yang, D., Nozaki, T.: Comparative study on the localized surface plasmon resonance of boron-and phosphorus-doped silicon nanocrystals. *ACS Nano* **9**(1), 378–386 (2015)

Zolfaghary pour, S., Arik, K.: Ultra-broadband polarization-independent perfect absorber based on phase change material ($\text{Ge}_2\text{Sb}_2\text{Te}_5$ or GST) for the visible and infrared regions. *Opt. Quantum Electron.* 55(2), 141 (2023). <https://doi.org/10.1007/s11082-022-04395-z>

Publisher's Note Springer Nature remains neutral with regard to jurisdictional claims in published maps and institutional affiliations.